nature

Supplementary Information for

Dynamics of growing carbon nanotube interfaces probed by machine learning-enabled molecular simulations

Daniel Hedman, Ben McLean, Christophe Bichara, Shigeo Maruyama, J. Andreas Larsson and Feng Ding

Corresponding authors: Daniel Hedman, daniel.hedman@ltu.se; Feng Ding, f.ding@siat.ac.cn

Here, additional information is presented to support the results in the main text. This includes evaluation of the accuracy of the DeepCNT-22 MLFF and details of the five phases of nanotube growth. As well as derivation of the probability density function, cumulative distribution function and expected value of τ and derivation of the simple model to predict $\langle N_{\mathrm{C}} \rangle$.

1. Validation of DeepCNT-22

Validating the accuracy of MLFFs is a crucial step for which multiple methods have been proposed[1]. In this case, the energy and force accuracy of DeepCNT-22 is evaluated on a subset of structures, constituting 10% of the entire dataset shown in Fig. 1 in the main text. On this test set (not used in the training process), the root mean square error (RMSE) of the energy and force predictions from DeepCNT-22 was calculated. The regression plots in Fig. S1a and 1b show that DeepCNT-22 can reproduce the DFT energies and forces of the test dataset with an RMSE of 13.51 meV per atom for energies and 325.48 meV/Å for forces, comparable to other published MLFFs based on the same architecture[2, 3].

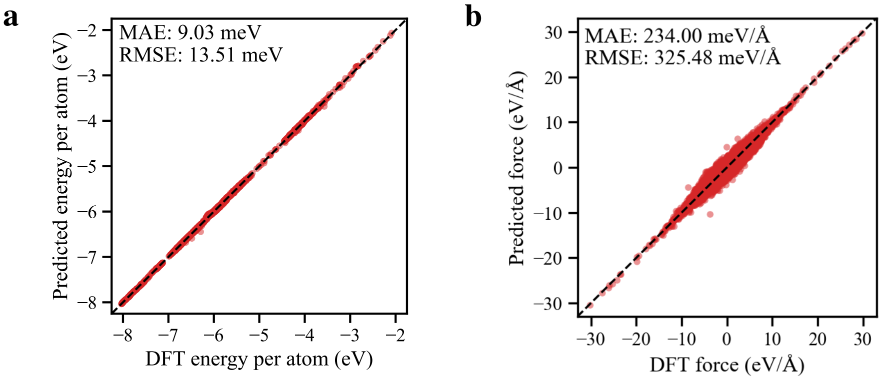

Fig. S1. Regression plots for the **a** energy and **b** force predictions of DeepCNT-22 evaluated on the test data. The test data is a 10% subset of the DeepCNT-22 dataset, which was kept separate during the MLFF training process.

Apart from validating the accuracy in energy and forces of DeepCNT-22, it is essential to ensure that the MLFF can reproduce known physical properties of the target system. To this end, DeepCNT-22's ability to reproduce the subtle energy difference of SWCNTs with varying curvature, i.e., the SWCNT curvature energy, E_c, is examined. Previous studies[4] have shown that this energy can be described as a function of the curvature, $1/R$, of a SWCNT of radius R as $E_c = \gamma \cdot (1/R)^2$. Here a value of $\gamma = 2.038$ eVÅ^2 obtained via previous DFT calculations[5] was used. As shown in Fig. S2a, DeepCNT-22 can reproduce the curvature energy of SWCNTs over a wide diameter range with high accuracy.

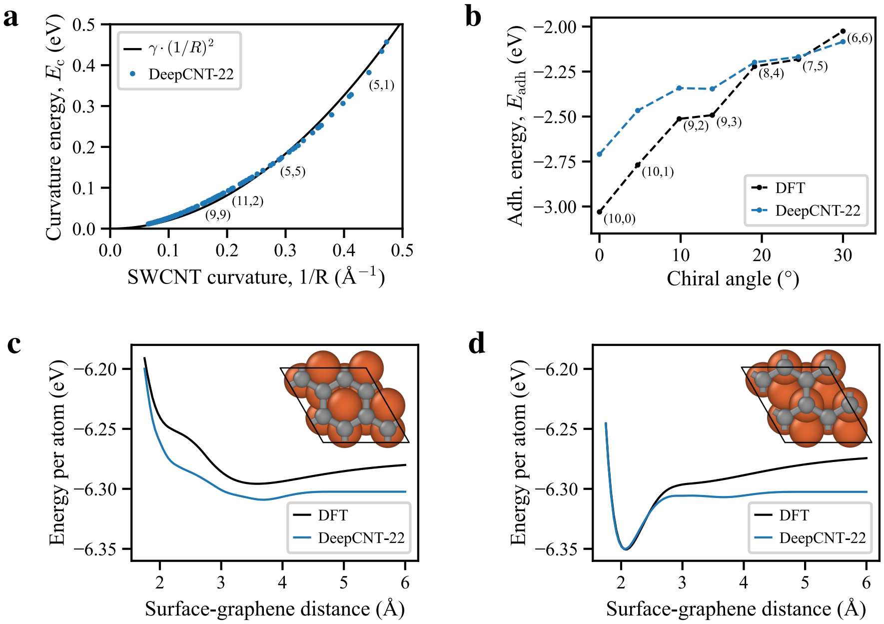

Fig. S2. Validation of DeepCNT-22's ability to accurately reproduce properties related to growth. **a** the curvature energy for SWCNTs, computed with DeepCNT-22, compared to the known analytical expression fitted to DFT energies. **b** the carbon-metal adhesion energy of SWCNTs attached to "clean" iron clusters, calculated using both DeepCNT-22 and DFT. **c** and **d** the 1D potential energy surface of graphene adsorbed on an Fe(111) surface in the fcc–hollow and fcc-top configurations, respectively.

Furthermore, DeepCNT-22's ability to reproduce the carbon-metal adhesion energy[6–8] of SWCNTs with various chiralities attached to Fe$_{55}$ clusters is evaluated. The adhesion energy of a SWCNT with chirality n, m is calculated as $E^{n,m}_{\text{adh}} = \left(E^{n,m}_{\text{cx}} - \left(E_{\text{Fe}_{55}} + E^{n,m}\right)\right)/(n+m)$, where $E^{n,m}_{\text{cx}}$ is the energy of the complex (SWCNT attached to a Fe$_{55}$ cluster), $E_{\text{Fe}_{55}}$ is the energy of the cluster itself, and $E^{n,m}$ is the energy of the SWCNT. As shown in Fig. S2b, DeepCNT-22 can reproduce the trend in the carbon-metal adhesion energy as a function of the tube's chirality. While an exact agreement with DFT is not reached, DeepCNT-22's ability to reproduce this trend is noteworthy, given that the training data does not contain structures of SWCNTs attached to "clean" Fe clusters, i.e., clusters with no carbon atoms dissolved, as well as no structures of open-ended SWCNTs. This indicates that DeepCNT-22 can generalize reasonable well to structures outside of the training data.

An important property for SWCNT growth is the adhesion strength between graphitic carbon and the metal surface, as it affects SWCNT-cap lift off versus encapsulation of the catalyst[9]. Fig. S2c and 2d shows the 1D potential energy surface of graphene adsorbed on an Fe(111) surface in the fcc–hollow and fcc-top configurations, respectively. As shown, DeepCNT-22 can reproduce both the shallow minimum for the fcc–hollow and the deeper minimum for the fcc-top configuration. It is important to note that the adhesion energy for DeepCNT-22 plateaus at around 5.0 Å, as this is the cutoff used for the MLFF.

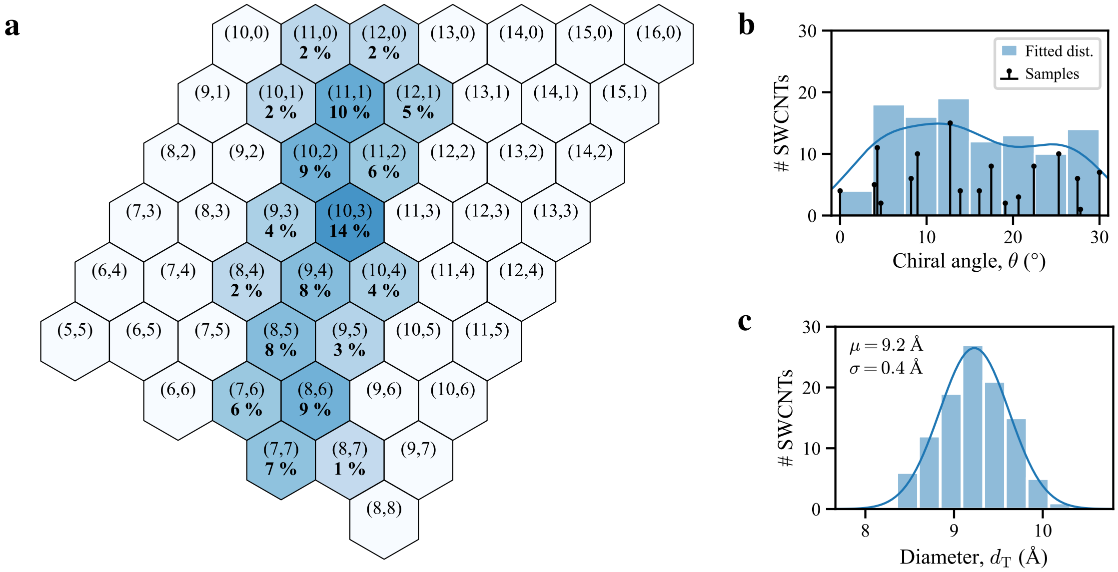

Fig. S3. Chirality distribution of 106 SWCNTs grown using a Fe_{55} catalyst at $T = 1300$ K and a carbon supply rate of $k = 0.5$ ns^{-1}. **a** the chirality map showing the abundance of each chirality (n, m) observed post-growth. **b** and **c** depict the distributions of the chiral angle and SWCNT diameter, respectively.

Experiments have shown that when SWCNTs are grown using Fe catalysts and simple hydrocarbon feedstock gas, the final product exhibits a broad chirality distribution[10, 11]. To evaluate DeepCNT-22's ability to accurately describe the nucleation of SWCNTs, where chirality is set, 280 growth simulations were conducted under identical conditions: Fe_{55} catalyst, 1300K growth temperature, and 200 carbon atoms supplied at a rate of $k = 0.5$ ns^{-1}. These simulations resulted in 106 SWCNTs with well-defined chirality which are shown in Fig. S5, corresponding to a yield of 37.9%. The remaining 174 SWCNTs, with undefinable chirality, are shown in Fig. S6. Here, a variety of failure modes can be seen such as: "Cap liftoff failure" where the SWCNT-cap fails to lift from the catalyst causing encapsulation. "Cap formation failure" where a conical cap is formed which causes the diameter of the graphite structure to continue to increase/decrease until a size limit is reached, as determined by the size of the catalyst. "Defect induced failure" where an interfacial defect becomes trapped inside the tube wall during growth causing a change in chirality. Note that all of these failure modes are the result of an inappropriate number of penta- or heptagons forming the graphite structure. A broad chirality distribution is expected for these growth conditions, and as observed in the chiral map in Fig. S3a and in the distribution of the chiral angles in Fig. S3b this is indeed the case for SWCNTs grown with DeepCNT-22. Impressively, the diameter distribution of the grown tubes, as shown in Fig. S3c, agrees well with the experimental results of Ago et al.[12], who grew SWCNTs on Fe catalysts of size 1.5-3 nm.

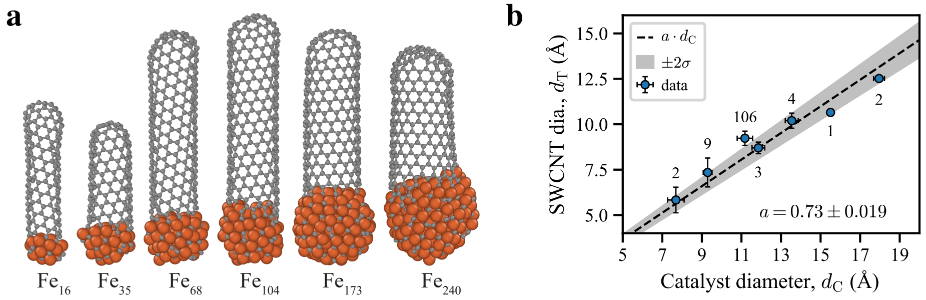

Fig. S4. SWCNTs grown on Fe catalysts with varying diameters, d_C. **a** shows an example of the structures obtained after growth. **b** is resulting tube diameters, d_T, which follow a linear relationship $d_T = a \cdot d_C$ with $a = 0.73 \pm 0.019$. Here, the gray bands indicate the 2σ confidence interval of the fit and the number of SWCNTs grown for each catalyst size is marked above the data points.

Like the chirality distribution, another crucial property of growth to reproduce is the ratio between the diameter of the grown tube and that of the catalyst. Previous growth experiments[13, 14] and theoretical studies[15, 16] have established a link between the tube diameter and the catalyst diameter, where the tube diameter is between 0.7-1.0 times the catalyst diameter. Fig. S4a displays a selection of tubes grown using DeepCNT-22 on Fe catalysts of varying sizes, where it is evident that the diameter of the tube increases with the diameter of the catalyst. To quantify this, multiple growth simulations where performed on catalysts of different sizes. Here the growth temperature was set to $T = 1300$ K for each catalyst size, but the total number of carbon atoms added and the supply rate, k, was adjusted for each catalyst size to achieve growth. Fig. S4b illustrates the mean SWCNT diameter as a function of the mean catalyst diameter, where a linear relationship can be found $d_T = a \cdot d_C$, with $a = 0.73 \pm 0.019$, in agreement with previous studies.

2. The five phases of nanotube growth

The growth process of the $(6, 5)$ SWCNT can be observed in Fig. 2A of the main text and Extended Data Video 1, revealing the following. In the earliest (1^{st}) phase of growth, monomers and dimers are the dominant carbon species. This observation is supported by the snapshot at $t = 8.80$ ns and the carbon species analysis presented in Fig. 2B of the main text, indicating that almost no carbon chains are present on the catalyst during the 1^{st} phase. Notably, the high carbon supply rate employed at the beginning of growth, $k = 5$ ns^{-1}, leads to a significantly shorter 1^{st} phase compared to using a slower rate of $k = 0.5$ ns^{-1}.

The 2^{nd} phase of growth is characterized by the transformation of carbon monomers and dimers into linear carbon chains, as seen in the snapshot structure at $t = 28.4$ ns and the steady increase in the number of carbon atoms within chains, as shown in Fig. 2B. After reaching a critical ratio of approximately 1/3 carbon atoms as part of chains, the growth enters the 3^{rd} phase. Here, a junction forms on a long chain when a monomer, dimer, or the end of another chain attaches, creating a three-coordinated carbon atom. This action causes the resulting chain-like structure to fold and form the first carbon ring, as seen in the snapshot at $t = 34.25$ ns. The creation of the first carbon ring facilitates rapid subsequent ring formation, evidenced by the sharp decrease in the number of atoms in chains and the simultaneous sharp increase in the number of graphitic carbons shown in Fig. 2B. As a result, linear carbon chains are almost entirely eliminated (Fig. 2B) as they become part of the growing graphitic structure seen at $t = 39.60$ ns.

Following this, the growth enters the 4th phase, in which the graphitic structure enlarges as carbon monomers and dimers attach to its edge. As the graphitic structure expands, its curvature increases, and due to the energetic advantage of a near-perpendicular interface between the catalyst and the graphitic structure[9], it lifts off the catalyst. The SWCNT-cap is fully defined once at least six pentagons form inside the graphitic structure[17], which occurs at $t = 132.41$ ns. Subsequently, the growth enters the 5th and final phase, characterized by the continuous elongation of the tube through the attachment of carbon atoms at its edge.

3. Derivation of the PDF, CDF and expected value of τ

As observed in Fig. 1F of the main text τ follows a power-law distribution ($\tau^{-\alpha}$) with an exponential cutoff ($e^{-\lambda_2 \tau}$). This distribution's probability density function (PDF) can be expressed as

$$f_\tau(\tau) = C \cdot \tau^{-\alpha} \cdot e^{-\lambda_2 \tau} \tag{S1}$$

and must satisfy the following normalization constraint

$$\int_{\tau_{\text{min}}}^{\infty} C \cdot \tau^{-\alpha} \cdot e^{-\lambda_2 \tau} \, d\tau = 1. \tag{S2}$$

This constraint leads to a normalization constant of

$$C = \frac{1}{\int_{\tau_{\text{min}}}^{\infty} \tau^{-\alpha} \cdot e^{-\lambda_2 \tau} \, d\tau} = \frac{\lambda_2^{1-\alpha}}{\Gamma\left(1-\alpha, \lambda_2 \tau_{\text{min}}\right)}, \tag{S3}$$

here $\Gamma\left(1-\alpha, \lambda_2 \tau_{\text{min}}\right)$ is the upper incomplete gamma function. From the PDF defined in Eq. (S1), the cumulative distribution function (CDF) can then be determined

$$F_\tau(\tau) = \int_{\tau_{\text{min}}}^{\tau} f_\tau(x) \, dx = 1 - \frac{\Gamma\left(1-\alpha, \lambda_2 \tau\right)}{\Gamma\left(1-\alpha, \lambda_2 \tau_{\text{min}}\right)}. \tag{S4}$$

Lastly, the expected value for τ can be determined using Eq. (S1)

$$\langle \tau \rangle = \int_{\tau_{\text{min}}}^{\infty} \tau f_\tau(\tau) \, d\tau = \frac{1}{\lambda_2} \frac{\Gamma\left(2-\alpha, \lambda_2 \tau_{\text{min}}\right)}{\Gamma\left(1-\alpha, \lambda_2 \tau_{\text{min}}\right)}. \tag{S5}$$

4. Derivation of $\langle N_{\text{D}} \rangle$ and $\langle N_{\text{C}} \rangle$

As mentioned in the main text a straightforward model is proposed to determine the expected length of a CNT in terms of the number of carbon atoms, $\langle N_C \rangle$, that can be reached during growth before an interface defect is likely to become trapped in the tube wall. Assume that n_6 hexagons need to form at the interface of the growing tube to trap an interface defect. Given a growth rate, k, the average formation rate of hexagons during growth equals $k_6 = k/2$, as shown in Fig. 2C of the main text. Consequently, the critical time that an interface defect must live to become trapped inside the tube wall can be expressed as

$$\tau_c = \frac{n_6}{k_6} = \frac{2n_6}{k}. \tag{S6}$$

Since the CDF, F_τ, for the interface defect lifetimes is known (Eq. (S4)), the probability, p, that an interface defect lives for at least time τ_c can be calculated using the survival function

$$p = S_\tau(\tau_c) = 1 - F_\tau(\tau_c) = \frac{\Gamma(1-\alpha,\ \lambda_2\tau_c)}{\Gamma(1-\alpha,\ \lambda_2\tau_{\min})}. \tag{S7}$$

With the probability, p, it becomes possible to calculate how many interface defects are expected to be created before one has a lifetime of at least τ_c

$$\langle N_\mathrm{D}\rangle = \frac{1}{p} = \frac{\Gamma(1-\alpha,\ \lambda_2\tau_{\min})}{\Gamma(1-\alpha,\ \lambda_2\tau_c)}. \tag{S8}$$

Since $\langle N_D\rangle$ is independent of the expected time between the formation of interface defects, $\langle \delta t\rangle$, and the supply rate of carbon atoms, k, is known, the number of carbon atoms expected to be added to the growing tube before an interface defect becomes trapped can be calculated as

$$\langle N_\mathrm{C}\rangle = \langle N_\mathrm{D}\rangle \cdot \langle \delta t\rangle \cdot k = \frac{k}{\lambda_1}\frac{\Gamma(1-\alpha,\ \lambda_2\tau_{\min})}{\Gamma\left(1-\alpha,\ \lambda_2\frac{2n_6}{k}\right)}. \tag{S9}$$

Now to calculate $\langle N_C\rangle$ using Eq. (S9), an initial value for n_6 must be assumed. Considering the worst-case scenario, in which an interface defect is formed such that only one hexagon needs to be added to the interface of the growing tube to trap the defect, $n_6 = 1$ can be assumed. This assumption can be verified using Eq. (S8) with parameter values for the interface defect formation and lifetime distributions obtained from the growth of the $(6,5)$ SWCNT shown in Fig. 2 of the main text: $\lambda_1 = 1.08 \cdot 10^9$ s^{-1}, $\alpha = 1.20$, $\lambda_2 = 1.04 \cdot 10^9$ s^{-1}, $\tau_{\min} = 1.10 \cdot 10^{-12}$ s, and $k = 0.5$ ns^{-1}. This yields $\langle N_D\rangle \approx 6000$ interface defects expected to form before one gets trapped inside the tube wall, significantly more than the 804 interface defects observed during growth, Sim. 1 in Extended Data Table 1. For a carbon supply rate of $k = 5$ ns^{-1}, ten times the value used to grow the $(6,5)$ SWCNT, $\langle N_D\rangle \approx 20$ and $\langle N_C\rangle \approx 90$ are obtained. Which demonstrates that at these high growth rates, interface defects are likely to live long enough to get trapped inside the tube wall, resulting in a defective CNT. This is consistent with simulations at similar growth rates, which yielded defective tubes, and confirms that $n_6 = 1$ is a reasonable assumption. It should be noted that Eq. (S9) with $n_6 = 1$ is identical to Eq. (3) in the main text.

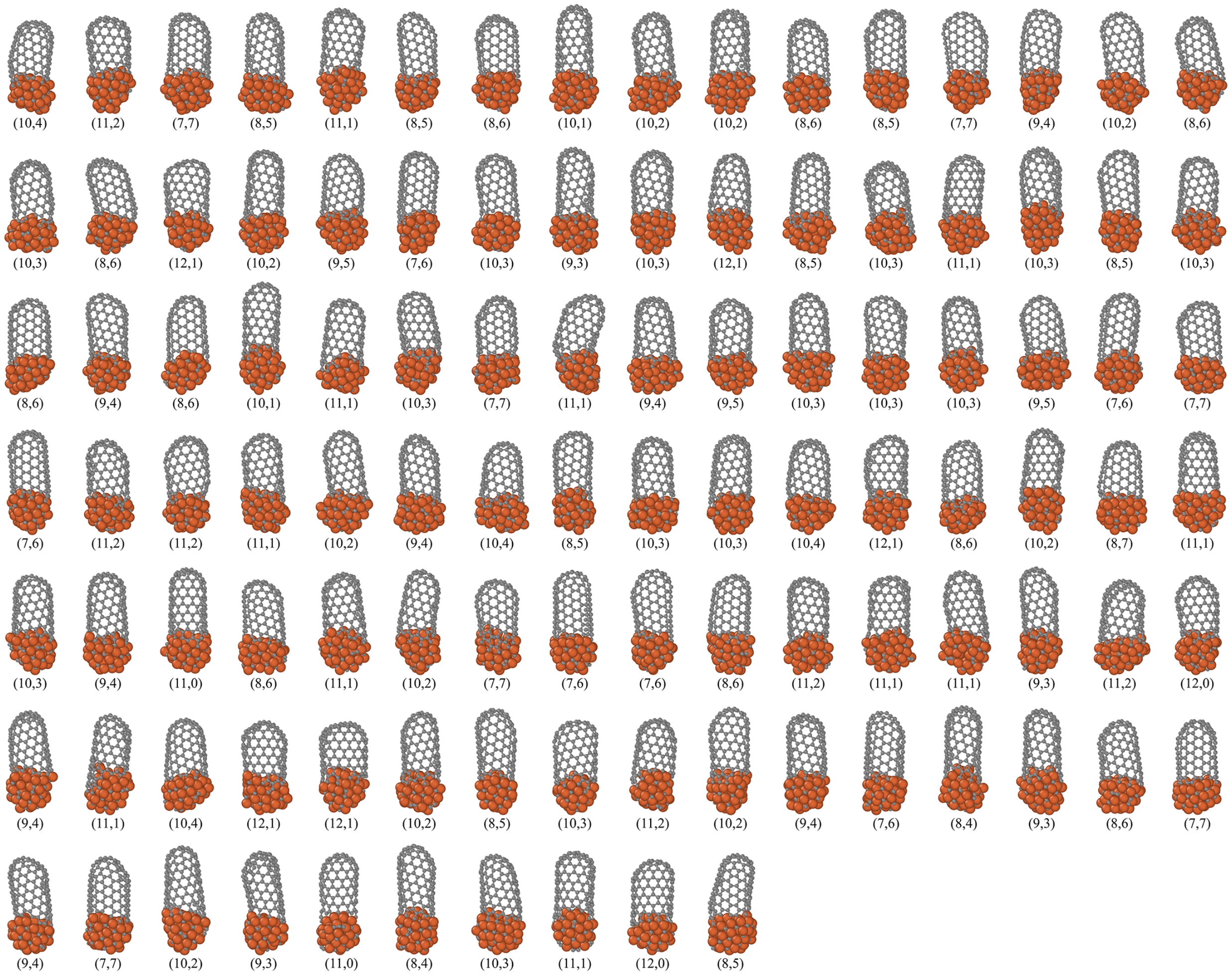

Fig. S5. The structure of the 106 SWCNTs with well-defined chirality obtained after growth and analyzed in Fig. S3. The chirality (n, m) of each tube is marked below.

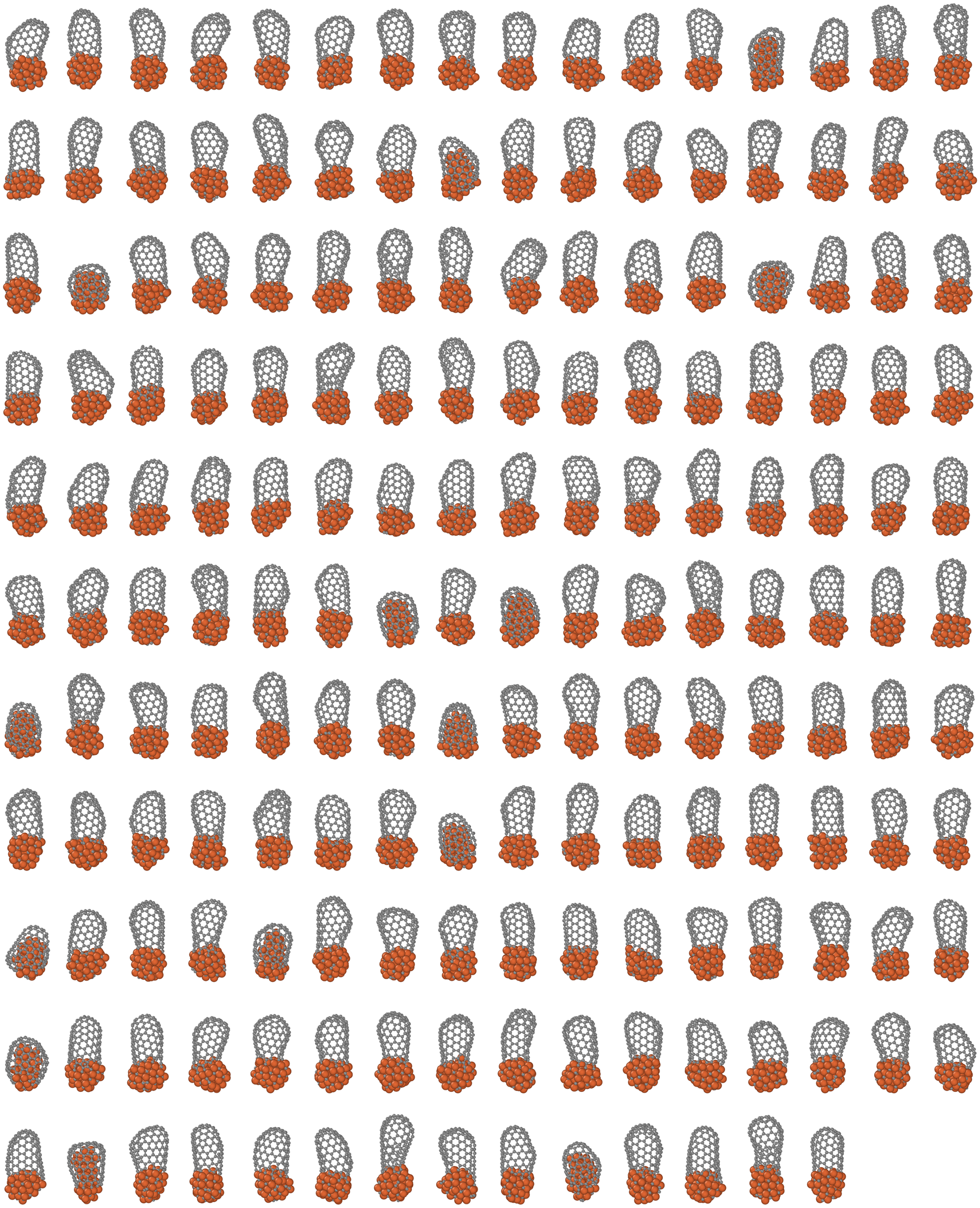

Fig. S6. The structure of the 174 SWCNTs with undefinable chirality obtained after growth. Here various failure modes can be seen.

References

1. Morrow, J. D., Gardner, J. L. A. & Deringer, V. L. How to validate machine-learned interatomic potentials. *The Journal of chemical physics* **158,** 121501. https://doi.org/10.1063/5.0139611 (Mar. 2023).
2. Zeng, J., Cao, L., Xu, M., Zhu, T. & Zhang, J. Z. H. Complex reaction processes in combustion unraveled by neural network-based molecular dynamics simulation. *Nature communications* **11,** 5713. https://doi.org/10.1038/s41467-020-19497-z (Nov. 2020).
3. Zeng, J., Zhang, L., Wang, H. & Zhu, T. Exploring the Chemical Space of Linear Alkane Pyrolysis via Deep Potential GENerator. *Energy & Fuels* **35,** 762–769. https://doi.org/10.1021/acs.energyfuels.0c03211 (Dec. 2020).
4. Kudin, K. N., Scuseria, G. E. & Yakobson, B. I. $\mathrm{C_2F}$, BN, and C nanoshell elasticity from ab initio computations. *Physical Review B* **64,** 235406. https://doi.org/10.1103/PhysRevB.64.235406 (Nov. 2001).
5. Hedman, D. & Larsson, J. A. Analytical modelling of single-walled carbon nanotube energies: the impact of curvature, length and temperature. *SN Applied Sciences* **2.** https://doi.org/10.1007/s42452-020-2139-z (Feb. 2020).
6. Larsson, P. *et al.* Calculating carbon nanotube-catalyst adhesion strengths. *Physical Review B* **75,** 115419. https://doi.org/10.1103/PhysRevB.75.115419 (Mar. 2007).
7. Ding, F. *et al.* The Importance of Strong Carbon-Metal Adhesion for Catalytic Nucleation of Single-Walled Carbon Nanotubes. *Nano Letters* **8,** 463–468. https://doi.org/10.1021/nl072431m (Dec. 2007).
8. Silvearv, F., Larsson, P., Jones, S. L. T., Ahuja, R. & Larsson, J. A. Establishing the most favorable metal-carbon bond strength for carbon nanotube catalysts. *Journal of Materials Chemistry C* **3,** 3422–3427. https://doi.org/10.1039/C5TC00143A (2015).
9. Ding, L. P. *et al.* Why Carbon Nanotubes Grow. *Journal of the American Chemical Society* **144,** 5606–5613. https://doi.org/10.1021/jacs.2c00879 (Mar. 2022).
10. Chiang, W.-H. & Sankaran, R. M. Linking catalyst composition to chirality distributions of as-grown single-walled carbon nanotubes by tuning Ni(x)Fe(1-x) nanoparticles. *Nature Materials* **8,** 882–886. https://doi.org/10.1038/nmat2531 (Sept. 2009).
11. He, M., Jiang, H., Kauppinen, E. I. & Lehtonen, J. Diameter and chiral angle distribution dependencies on the carbon precursors in surface-grown single-walled carbon nanotubes. *Nanoscale* **4,** 7394–7398. DOI%09https://doi.org/10.1039/C2NR32276E (Oct. 2012).
12. Ago, H. *et al.* CVD Growth of Single-Walled Carbon Nanotubes with Narrow Diameter Distribution over Fe/MgO Catalyst and Their Fluorescence Spectroscopy. *The Journal of Physical Chemistry B* **109,** 10035–10041. https://doi.org/10.1021/jp050307q (May 2005).

13. Diaz, M. C., Jiang, H., Kauppinen, E., Sharma, R. & Balbuena, P. B. Can Single-Walled Carbon Nanotube Diameter Be Defined by Catalyst Particle Diameter? *The Journal of Physical Chemistry C* **123,** 30305–30317. `https://doi.org/10.1021/acs.jpcc.9b07724` (Dec. 2019).
14. Yang, F. *et al.* Growth modes of single-walled carbon nanotubes on catalysts. *Science advances* **8,** eabq0794. `https://doi.org/10.1126/sciadv.abq0794` (Oct. 2022).
15. Ding, F., Rosén, A. & Bolton, K. Molecular dynamics study of the catalyst particle size dependence on carbon nanotube growth. *The Journal of chemical physics* **121,** 2775–2779. `https://doi.org/10.1063/1.1770424` (July 2004).
16. Xu, Z. & Ding, F. Catalyst particle size dependent carbon nanotube cloning. *Carbon* **175,** 69–76. `https://doi.org/10.1016/j.carbon.2020.12.085` (Apr. 2021).
17. Xu, Z., Qiu, L. & Ding, F. The kinetics of chirality assignment in catalytic single-walled carbon nanotube growth and the routes towards selective growth. *Chemical Science* **9,** 3056–3061. `https://doi.org/10.1039/C7SC04714B` (2018).